Measurements of D^0 and D^* production in $p + p$ collisions at $\sqrt{s} = 200$ GeV

L. Adamczyk,[1] G. Agakishiev,[19] M. M. Aggarwal,[30] Z. Ahammed,[49] A. V. Alakhverdyants,[19] I. Alekseev,[17] J. Alford,[20] B. D. Anderson,[20] C. D. Anson,[28] D. Arkhipkin,[3] E. Aschenauer,[3] G. S. Averichev,[19] J. Balewski,[24] A. Banerjee,[49] Z. Barnovska,[12] D. R. Beavis,[3] R. Bellwied,[45] M. J. Betancourt,[24] R. R. Betts,[9] A. Bhasin,[18] A. K. Bhati,[30] H. Bichsel,[51] J. Bielcik,[11] J. Bielcikova,[12] L. C. Bland,[3] I. G. Bordyuzhin,[17] W. Borowski,[42] J. Bouchet,[20] A. V. Brandin,[27] S. G. Brovko,[5] E. Bruna,[53] S. Bueltmann,[29] I. Bunzarov,[19] T. P. Burton,[3] J. Butterworth,[37] X. Z. Cai,[41] H. Caines,[53] M. Calderón de la Barca Sánchez,[5] D. Cebra,[5] R. Cendejas,[6] M. C. Cervantes,[43] P. Chaloupka,[12] S. Chattopadhyay,[49] H. F. Chen,[39] J. H. Chen,[41] J. Y. Chen,[8] L. Chen,[8] J. Cheng,[46] M. Cherney,[10] A. Chikanian,[53] W. Christie,[3] P. Chung,[12] J. Chwastowski,[43] M. J. M. Codrington,[43] R. Corliss,[24] J. G. Cramer,[51] H. J. Crawford,[4] X. Cui,[39] A. Davila Leyva,[44] L. C. De Silva,[45] R. R. Debbe,[3] T. G. Dedovich,[19] J. Deng,[40] R. Derradi de Souza,[7] S. Dhamija,[16] L. Didenko,[3] F. Ding,[5] A. Dion,[3] P. Djawotho,[43] X. Dong,[23] J. L. Drachenberg,[43] J. E. Draper,[5] C. M. Du,[22] L. E. Dunkelberger,[6] J. C. Dunlop,[3] L. G. Efimov,[19] M. Elnimr,[52] J. Engelage,[4] G. Eppley,[37] L. Eun,[23] O. Evdokimov,[9] R. Fatemi,[21] S. Fazio,[3] J. Fedorisin,[19] R. G. Fersch,[21] P. Filip,[19] E. Finch,[53] Y. Fisyak,[3] C. A. Gagliardi,[43] D. R. Gangadharan,[28] F. Geurts,[37] S. Gliske,[2] Y. N. Gorbunov,[10] O. G. Grebenyuk,[23] D. Grosnick,[48] S. Gupta,[18] W. Guryn,[3] B. Haag,[5] O. Hajkova,[11] A. Hamed,[43] L-X. Han,[41] J. W. Harris,[53] J. P. Hays-Wehle,[24] S. Heppelmann,[32] A. Hirsch,[34] G. W. Hoffmann,[44] D. J. Hofman,[9] S. Horvat,[53] B. Huang,[3] H. Z. Huang,[6] P. Huck,[8] T. J. Humanic,[28] L. Huo,[43] G. Igo,[6] W. W. Jacobs,[16] C. Jena,[14] J. Joseph,[20] E. G. Judd,[4] S. Kabana,[42] K. Kang,[46] J. Kapitan,[12] K. Kauder,[9] H. W. Ke,[8] D. Keane,[20] A. Kechechyan,[19] A. Kesich,[5] D. Kettler,[51] D. P. Kikola,[34] J. Kiryluk,[23] A. Kisiel,[50] V. Kizka,[19] S. R. Klein,[23] D. D. Koetke,[48] T. Kollegger,[13] J. Konzer,[34] I. Koralt,[29] L. Koroleva,[17] W. Korsch,[21] L. Kotchenda,[27] P. Kravtsov,[27] K. Krueger,[2] L. Kumar,[20] M. A. C. Lamont,[3] J. M. Landgraf,[3] S. LaPointe,[52] J. Lauret,[3] A. Lebedev,[3] R. Lednicky,[19] J. H. Lee,[3] W. Leight,[24] M. J. LeVine,[3] C. Li,[39] L. Li,[44] W. Li,[41] X. Li,[34] X. Li,[40] Y. Li,[46] Z. M. Li,[8] L. M. Lima,[38] M. A. Lisa,[28] F. Liu,[8] T. Ljubicic,[3] W. J. Llope,[37] R. S. Longacre,[3] Y. Lu,[39] X. Luo,[8] A. Luszczak,[41] G. L. Ma,[41] Y. G. Ma,[41] D. M. M. D. Madagodagettige Don,[10] D. P. Mahapatra,[14] R. Majka,[53] O. I. Mall,[5] S. Margetis,[20] C. Markert,[44] H. Masui,[23] H. S. Matis,[23] D. McDonald,[37] T. S. McShane,[10] S. Mioduszewski,[43] M. K. Mitrovski,[3] Y. Mohammed,[43] B. Mohanty,[49] B. Morozov,[17] M. G. Munhoz,[38] M. K. Mustafa,[34] M. Naglis,[23] B. K. Nandi,[15] Md. Nasim,[49] T. K. Nayak,[49] L. V. Nogach,[33] J. Novak,[26] G. Odyniec,[23] A. Ogawa,[3] K. Oh,[35] A. Ohlson,[53] V. Okorokov,[27] E. W. Oldag,[44] R. A. N. Oliveira,[38] D. Olson,[23] P. Ostrowski,[50] M. Pachr,[11] B. S. Page,[16] S. K. Pal,[49] Y. X. Pan,[6] Y. Pandit,[20] Y. Panebratsev,[19] T. Pawlak,[50] B. Pawlik,[31] H. Pei,[9] C. Perkins,[4] W. Peryt,[50] P. Pile,[3] M. Planinic,[54] J. Pluta,[50] D. Plyku,[29] N. Poljak,[54] J. Porter,[23] A. M. Poskanzer,[23] C. B. Powell,[23] D. Prindle,[51] C. Pruneau,[52] N. K. Pruthi,[30] M. Przybycien,[1] P. R. Pujahari,[15] J. Putschke,[52] H. Qiu,[23] R. Raniwala,[36] S. Raniwala,[36] R. L. Ray,[44] R. Redwine,[24] R. Reed,[5] C. K. Riley,[53] H. G. Ritter,[23] J. B. Roberts,[37] O. V. Rogachevskiy,[19] J. L. Romero,[5] J. F. Ross,[10] L. Ruan,[3] J. Rusnak,[12] N. R. Sahoo,[49] I. Sakrejda,[23] S. Salur,[23] A. Sandacz,[50] J. Sandweiss,[53] E. Sangaline,[5] A. Sarkar,[15] J. Schambach,[44] R. P. Scharenberg,[34] A. M. Schmah,[23] B. Schmidke,[3] N. Schmitz,[25] T. R. Schuster,[13] J. Seele,[24] J. Seger,[10] P. Seyboth,[25] N. Shah,[6] E. Shahaliev,[19] M. Shao,[39] B. Sharma,[30] M. Sharma,[52] S. S. Shi,[8] Q. Y. Shou,[41] E. P. Sichtermann,[23] R. N. Singaraju,[49] M. J. Skoby,[34] D. Smirnov,[3] N. Smirnov,[53] D. Solanki,[36] P. Sorensen,[3] U. G. deSouza,[38] H. M. Spinka,[2] B. Srivastava,[34] T. D. S. Stanislaus,[48] S. G. Steadman,[24] J. R. Stevens,[16] R. Stock,[13] M. Strikhanov,[27] B. Stringfellow,[34] A. A. P. Suaide,[38] M. C. Suarez,[9] M. Sumbera,[12] X. M. Sun,[23] Y. Sun,[39] Z. Sun,[22] B. Surrow,[24] D. N. Svirida,[17] T. J. M. Symons,[23] A. Szanto de Toledo,[38] J. Takahashi,[7] A. H. Tang,[3] Z. Tang,[39] L. H. Tarini,[52] T. Tarnowsky,[26] D. Thein,[44] J. H. Thomas,[23] J. Tian,[41] A. R. Timmins,[45] D. Tlusty,[12] M. Tokarev,[19] T. A. Trainor,[51] S. Trentalange,[6] R. E. Tribble,[43] P. Tribedy,[49] B. A. Trzeciak,[50] O. D. Tsai,[6] J. Turnau,[31] T. Ullrich,[3] D. G. Underwood,[2] G. Van Buren,[3] G. van Nieuwenhuizen,[24] J. A. Vanfossen, Jr.,[20] R. Varma,[15] G. M. S. Vasconcelos,[7] F. Videbæk,[3] Y. P. Viyogi,[49] S. Vokal,[19] S. A. Voloshin,[52] A. Vossen,[16] M. Wada,[44] F. Wang,[34] G. Wang,[6] H. Wang,[26] J. S. Wang,[22] Q. Wang,[34] X. L. Wang,[39] Y. Wang,[46] G. Webb,[21] J. C. Webb,[3] G. D. Westfall,[26] C. Whitten, Jr.,[6,*] H. Wieman,[23] S. W. Wissink,[16] R. Witt,[47] W. Witzke,[21] Y. F. Wu,[8] Z. Xiao,[46] W. Xie,[34] K. Xin,[37] H. Xu,[22] N. Xu,[23] Q. H. Xu,[40] W. Xu,[6] Y. Xu,[39] Z. Xu,[3] L. Xue,[41] Y. Yang,[22] Y. Yang,[8] P. Yepes,[37] Y. Yi,[34] K. Yip,[3] I-K. Yoo,[35] M. Zawisza,[50] H. Zbroszczyk,[50] J. B. Zhang,[8] S. Zhang,[41] W. M. Zhang,[20] X. P. Zhang,[46] Y. Zhang,[39] Z. P. Zhang,[39] F. Zhao,[6] J. Zhao,[41] C. Zhong,[41] X. Zhu,[46] Y. H. Zhu,[41] and Y. Zoulkarneeva[19]

(STAR Collaboration)

[1]*AGH University of Science and Technology, Cracow, Poland*
[2]*Argonne National Laboratory, Argonne, Illinois 60439, USA*

[3]*Brookhaven National Laboratory, Upton, New York 11973, USA*
[4]*University of California, Berkeley, California 94720, USA*
[5]*University of California, Davis, California 95616, USA*
[6]*University of California, Los Angeles, California 90095, USA*
[7]*Universidade Estadual de Campinas, Sao Paulo, Brazil*
[8]*Central China Normal University (HZNU), Wuhan 430079, China*
[9]*University of Illinois at Chicago, Chicago, Illinois 60607, USA*
[10]*Creighton University, Omaha, Nebraska 68178, USA*
[11]*Czech Technical University in Prague, FNSPE, Prague, 115 19, Czech Republic*
[12]*Nuclear Physics Institute AS CR, 250 68 Řež/Prague, Czech Republic*
[13]*University of Frankfurt, Frankfurt, Germany*
[14]*Institute of Physics, Bhubaneswar 751005, India*
[15]*Indian Institute of Technology, Mumbai, India*
[16]*Indiana University, Bloomington, Indiana 47408, USA*
[17]*Alikhanov Institute for Theoretical and Experimental Physics, Moscow, Russia*
[18]*University of Jammu, Jammu 180001, India*
[19]*Joint Institute for Nuclear Research, Dubna, 141 980, Russia*
[20]*Kent State University, Kent, Ohio 44242, USA*
[21]*University of Kentucky, Lexington, Kentucky, 40506-0055, USA*
[22]*Institute of Modern Physics, Lanzhou, China*
[23]*Lawrence Berkeley National Laboratory, Berkeley, California 94720, USA*
[24]*Massachusetts Institute of Technology, Cambridge, Massachusetts 02139-4307, USA*
[25]*Max-Planck-Institut für Physik, Munich, Germany*
[26]*Michigan State University, East Lansing, Michigan 48824, USA*
[27]*Moscow Engineering Physics Institute, Moscow, Russia*
[28]*Ohio State University, Columbus, Ohio 43210, USA*
[29]*Old Dominion University, Norfolk, Virginia, 23529, USA*
[30]*Panjab University, Chandigarh 160014, India*
[31]*Institute of Nuclear Physics PAS, Cracow, Poland*
[32]*Pennsylvania State University, University Park, Pennsylvania 16802, USA*
[33]*Institute of High Energy Physics, Protvino, Russia*
[34]*Purdue University, West Lafayette, Indiana 47907, USA*
[35]*Pusan National University, Pusan, Republic of Korea*
[36]*University of Rajasthan, Jaipur 302004, India*
[37]*Rice University, Houston, Texas 77251, USA*
[38]*Universidade de Sao Paulo, Sao Paulo, Brazil*
[39]*University of Science and Technology of China, Hefei 230026, China*
[40]*Shandong University, Jinan, Shandong 250100, China*
[41]*Shanghai Institute of Applied Physics, Shanghai 201800, China*
[42]*SUBATECH, Nantes, France*
[43]*Texas A&M University, College Station, Texas 77843, USA*
[44]*University of Texas, Austin, Texas 78712, USA*
[45]*University of Houston, Houston, Texas, 77204, USA*
[46]*Tsinghua University, Beijing 100084, China*
[47]*United States Naval Academy, Annapolis, Maryland 21402, USA*
[48]*Valparaiso University, Valparaiso, Indiana 46383, USA*
[49]*Variable Energy Cyclotron Centre, Kolkata 700064, India*
[50]*Warsaw University of Technology, Warsaw, Poland*
[51]*University of Washington, Seattle, Washington 98195, USA*
[52]*Wayne State University, Detroit, Michigan 48201, USA*
[53]*Yale University, New Haven, Connecticut 06520, USA*
[54]*University of Zagreb, Zagreb, HR-10002, Croatia*

(Received 19 April 2012; revised manuscript received 15 October 2012; published 31 October 2012)

We report measurements of charmed-hadron (D^0, D^*) production cross sections at midrapidity in $p + p$ collisions at a center-of-mass energy of 200 GeV by the STAR experiment. Charmed hadrons were reconstructed via the hadronic decays $D^0 \to K^- \pi^+$, $D^{*+} \to D^0 \pi^+ \to K^- \pi^+ \pi^+$ and their charge conjugates, covering the p_T range of 0.6–2.0 and 2.0–6.0 GeV/c for D^0 and D^{*+}, respectively. From this analysis,

[*]Deceased.

the charm-pair production cross section at midrapidity is $d\sigma/dy|_{y=0}^{c\bar{c}} = 170 \pm 45(\text{stat})^{+38}_{-59}(\text{sys})\ \mu\text{b}$. The extracted charm-pair cross section is compared to perturbative QCD calculations. The transverse momentum differential cross section is found to be consistent with the upper bound of a fixed-order next-to-leading logarithm calculation.

DOI: 10.1103/PhysRevD.86.072013 PACS numbers: 25.75.−q, 25.75.Cj

I. INTRODUCTION

The primary goal of ultrarelativistic heavy-ion experiments at the Relativistic Heavy Ion Collider (RHIC) is to search for and characterize the new state of matter with partonic degrees of freedom, namely, the quark-gluon plasma, predicted by quantum chromodynamics (QCD) [1]. In high-energy collisions at RHIC, heavy quarks (c, b) are expected to be created from initial hard scatterings [2] and the relative changes in their masses are small by the strong interactions with the QCD medium [3]. Thus they carry clean information from the system at the early stage. The interaction between heavy quarks and the medium is sensitive to the medium dynamics; therefore, heavy quarks are suggested as an ''ideal'' probe to quantify the properties of the strongly interacting QCD matter [4–6]. Consequently, measurements of heavy-quark production over a wide transverse momentum (p_T) region in proton-proton ($p + p$) collisions are critical to provide a baseline for understanding the results from heavy-ion collisions. In particular, precise knowledge of the total charm production cross sections from $p + p$ to central heavy-ion collisions is critical to understand both open charm and charmonium production mechanisms in the quark-gluon plasma medium formed in central heavy-ion collisions at RHIC [7,8].

In elementary particle collisions, processes involving heavy quarks with masses much larger than the QCD scale (Λ_{QCD}) are, in principle, amenable to perturbative QCD (pQCD) calculations. For heavy-quark production cross sections at large momentum transfer Q^2, fixed-order next-to-leading logarithm (FONLL) pQCD calculations, where $p_T \gg m_c$, are expected to work reasonably well [9]. However, calculations of the charm cross section at low p_T become complicated because charm quarks cannot be treated as a massless flavor. Furthermore, in the low momentum transfer region there is a large uncertainty in the gluon density function, and the strong coupling constant increases dramatically. Thus, perturbative QCD calculations have little predictive power for the total charm cross section in high-energy hadron-hadron collisions [10]. In view of these theoretical issues, experimental measurements become necessary and in turn provide constraints that improve theoretical calculations.

Measurements of inclusive charm production have been carried out through two main approaches: (i) single leptons from heavy-flavor semileptonic decays and (ii) charmed hadrons from hadronic decays. The advantages of the first method include an experimentally triggerable observable and relatively large decay branching ratios, thus resulting in relatively large statistics. However, interpretations of the experimental results contain ambiguities because (a) leptons are produced by various charmed and bottomed hadron decays, and (b) heavy-flavor hadrons contributing to leptons at a certain p_T can come from a wide kinematic region due to the decay smearing. The second method suffers from a large combinatorial background when all particles from the collision vertex are included, without any reconstruction of the secondary weak-decay vertices. This background is particularly large (S/B is on the order of $1{:}10^3$) in heavy-ion collisions.

There are many measurements of the charm production cross section in low energy $p + p$ or $p + \text{A}$ collisions via both semileptonic and hadronic decays at CERN and Fermilab [11,12]. Results for the total charm cross sections (from measurements with reasonable extrapolations) are consistent with next-to-leading-order pQCD calculations. At high energies, the Collider Detector at Fermilab (CDF) Collaboration at the Tevatron measured the charmed-hadron cross sections at $p_T > 5\ \text{GeV}/c$ in $p + \bar{p}$ collisions at $\sqrt{s} = 1.96\ \text{TeV}$, and results for D^0, D^+ and D^{*+} mesons are consistent with the upper bounds of FONLL pQCD calculations [13]. At RHIC energies, charm production has been studied mainly via semileptonic decay electrons from $p + p$ to $\text{Au} + \text{Au}$ collisions [14–18]. The result from $p + p$ collisions is also consistent with the upper bound of FONLL pQCD calculations at $p_T(e) > 2\ \text{GeV}/c$. Measurements of the D^0 cross section by the reconstruction of hadronic decays were carried out in $d + \text{Au}$ collisions [14], but no measurement of the charmed-hadron production cross section in $p + p$ collisions has been made at RHIC until now.

In this paper, we report measurements from the STAR experiment of the charmed-hadron (D^0, D^*) production cross section at midrapidity in $p + p$ collisions at $\sqrt{s} = 200\ \text{GeV}$. Charmed hadrons, D^0 and D^*, were reconstructed via hadronic decays in the transverse momentum ranges of 0.6–2.0 and 2–6 GeV/c, respectively. The p_T differential production cross sections are compared to pQCD theoretical calculations, and a total charm cross section is extracted.

The paper is organized as follows: Section II describes the experimental setup, the data set, and the particle-identification method used in this analysis. Section III explains the hadronic reconstruction for D^0 and D^* mesons in detail. Section IV discusses the reconstruction efficiency, acceptance, and trigger and vertex corrections.

Details of the systematic uncertainties are discussed in Sec. V. The transverse momentum differential production cross section is presented in Sec. VI and it is compared with pQCD FONLL and PYTHIA [19] calculations. The results are summarized in Sec. VII.

II. EXPERIMENTAL SETUP

A. Detector apparatus

The data used in this analysis were recorded by the Solenoidal Tracker at RHIC (STAR) detector [20]. The STAR detector is a multipurpose spectrometer with large rapidity coverage. The major subsystems at midrapidity sit inside a solenoidal magnet which provides a uniform magnetic field of 0.5 T along the beam axis. Subsystems used in this analysis are the time projection chamber (TPC) [21], the time-of-flight (TOF) detector [22], the barrel and end cap electromagnetic calorimeters [23,24], and two trigger detector subsystems: the vertex position detector (VPD) [25] and the beam beam counters (BBCs) [26].

The TPC is the main tracking detector, covering the full azimuthal angle at pseudorapidity $|\eta| < 1$ for tracks crossing all 45 padrows [21]. It measures the charged-particle momenta and provides particle-identification (PID) capability via the ionization energy loss (dE/dx) in the TPC gas, allowing a clean separation between charged kaons and pions up to momentum $p \sim 0.6$ GeV/c. The barrel TOF detector is a newly installed subsystem, utilizing the multigap resistive plate chamber technology [22]. The full system consists of 120 trays covering the full azimuth at $|\eta| < 0.9$ surrounding the TPC cylinder. In the year 2009 run, 84 trays out of 120 for the full barrel were installed and used for this analysis. The TOF detector uses the timing recorded in the forward VPD as the start time to calculate the particle time of flight, which is combined with the momentum from the TPC to identify particles. The timing resolution of the TOF system, including the start timing resolution in $\sqrt{s} = 200$ GeV $p + p$ collisions, is about 110 ps, allowing separation of K and π up to $p \sim 1.5$ GeV/c. The barrel and end cap electromagnetic calorimeters are designed to identify electrons and photons, covering the full azimuthal angle at $|\eta| < 1$ and $1 < \eta < 2$, respectively [23,24]. They are fast-response detectors (< 100 ns) and were used to suppress the TPC pileup-track contribution in the event-vertex finder by matching with charged tracks from the TPC.

In addition to providing the start time for the barrel TOF detector, the VPD is also one of the trigger detectors in STAR. It has two parts surrounding the beam pipe, located on the east and west sides, 5.7 m away from the center of the STAR detector and covering $4.24 < |\eta| < 5.1$ [25]. The minimum-bias trigger was defined as a coincidence signal in the east and west VPDs and a selection was made on the vertex position along the beam axis (V_z) to be within 40 cm of the center of the STAR detector. The BBC [26] consists of two identical counters located on each side of the TPC covering full azimuth and $2.1 < |\eta| < 5.0$ in pseudorapidity. Each part consists of a set of hexagonal scintillator tiles grouped into a ring and mounted around the beam pipe at a distance of 3.7 m from the center of STAR. The BBC detector had been used to define the main minimum-bias trigger in $p + p$ collisions before the minimum-bias trigger was used in 2009. A small sample of BBC minimum-bias-triggered events were collected in 2009 to check for a trigger bias. Details of the minimum-bias trigger bias and correction will be discussed in Sec. IV.

B. Data sets and event selection

The data sample used in this analysis consisted of minimum-bias-triggered $p + p$ collisions at $\sqrt{s} =$ 200 GeV, recorded in 2009 by the STAR experiment at RHIC.

The intrinsic drift time for electrons from the center to one end of the TPC is on the order of 40 μs. Thus, in high-luminosity $p + p$ collisions, one TPC event usually contains tracks from collisions originating from nontriggered bunch crossings. These "pileup events" will lead to additional tracks recorded in the TPC, in addition to those from the triggered event. This effect was not significant in previous RHIC runs, but the increase in the collision rate during 2009 to several hundred kilohertz made this a significant effect. The V_z position from offline VPD data has a resolution of 2.5 cm for minimum-bias events, which can provide a useful constraint to select the real event that fired the trigger. Figure 1, upper panel, shows the correlation between the V_z positions from the TPC and the VPD. Events with TPC vertices along the diagonal correlated band are real ones that fired the VPD minimum-bias trigger. In Fig. 1, bottom panel, the solid black histogram shows the 1D V_z difference between the first TPC-determined vertex position and VPD-determined vertex position. By applying a V_z difference cut $|\Delta Vz| < 6$ cm, most of the TPC pileup events can be removed. There still remain random associated correlations that enter into this cut window ($\sim 7\%$ level, calculated using a two-Gaussian fit). To further suppress this contamination, we required the TPC event vertices to have at least two tracks that match with hits in the barrel and end cap electromagnetic calorimeters (this vertex is treated as a "good" vertex). The red dashed histogram in Fig. 1, bottom panel, shows the ΔVz distribution after this selection. The random associated pileup events in the V_z difference cut window are now suppressed to $\sim 2\%$ of the total, while the corresponding loss of real events is $\sim 15\%$. In total, 105×10^6 minimum-bias events were used in the charmed-hadron analysis.

C. Track reconstruction and particle identification

Charged-particle tracks are required to point within $|\eta| < 1$ in order minimize TPC acceptance effects during reconstruction. Tracks must have 15 out of a maximum of 45 points used in track fitting (nFitPts) and at least 52% of

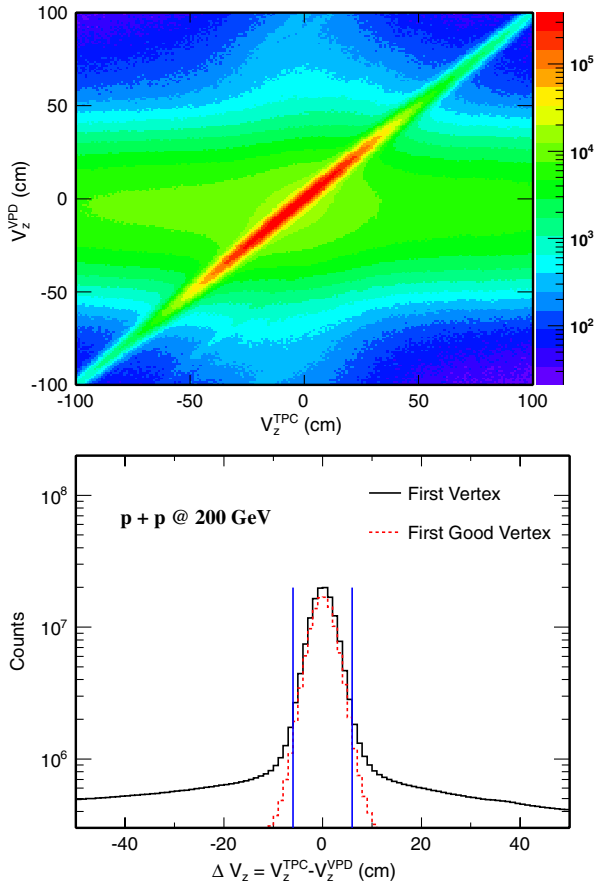

FIG. 1 (color online). Upper panel: Correlation of V_z^{TPC} versus V_z^{VPD}. Bottom panel: ΔV_z distributions. A good vertex requirement rejects most of the pileup events. Blue vertical lines indicate the cuts for the V_z selection.

the total possible fit points in order to avoid double-counting split tracks. Tracks are required to have a distance-of-closest-approach (DCA) to the collision vertex of less than 2 cm to suppress background tracks produced by secondary scattering in the detector and also long-lived particle decays. The STAR track pointing resolution with the TPC alone does not have the precision to separate charm secondary decay vertices from the collision vertices.

Particle identification for final-state charged hadrons was carried out with a combination of dE/dx in the TPC and the particle velocity (β) measurement from the barrel TOF detector. Thus the normalized $dE/dx(n\sigma_X^{dE/dx})$ and $1/\beta(n\sigma_X^{\mathrm{TOF}})$ distributions were used to select daughter particle candidates. They are defined as follows:

$$n\sigma_X^{dE/dx} = \frac{\ln \frac{\langle dE/dx \rangle^{\mathrm{mea}}}{dE/dx_X^{\mathrm{th}}}}{R_{dE/dx}}, \tag{1}$$

$$n\sigma_X^{\mathrm{TOF}} = \frac{\frac{1}{\beta^{\mathrm{mea}}} - \frac{1}{\beta_X^{\mathrm{th}}}}{R_{1/\beta}}, \tag{2}$$

where the superscripts "mea" and "th" are measured and theoretical values, respectively. The X denotes expected values which are calculated with respect to one kind of particle species (π or K). $R_{dE/dx}$ and $R_{1/\beta}$ are the experimental dE/dx and $1/\beta$ resolutions, respectively. With the above definitions, the two resulting distributions can be approximated by Gaussian distributions with mean ~ 0 and $\sigma \sim 1$). Figure 2 shows the $n\sigma_K^{dE/dx}$, $n\sigma_\pi^{dE/dx}$, and $n\sigma_K^{\mathrm{TOF}}$ distributions versus particle momentum.

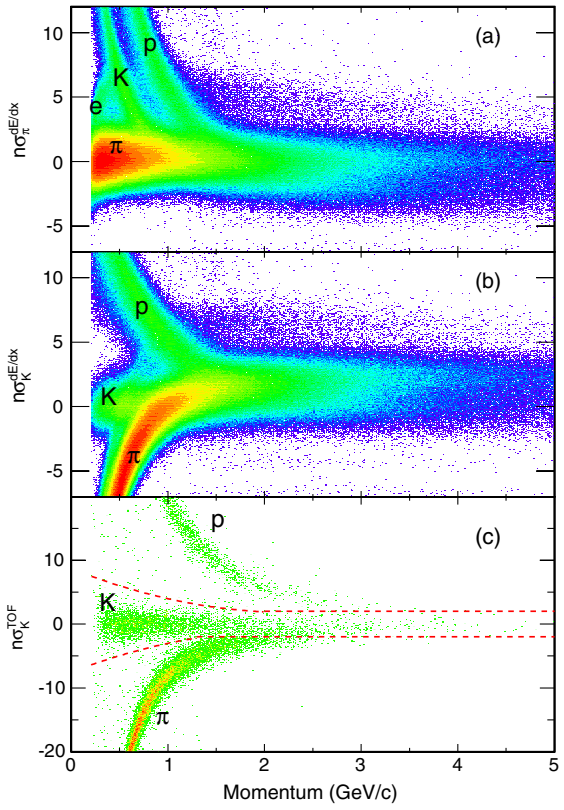

FIG. 2 (color online). Distributions of $n\sigma_\pi^{dE/dx}$, $n\sigma_K^{dE/dx}$, and $n\sigma_K^{\mathrm{TOF}}$ versus momentum are shown in panels (a), (b), and (c), respectively. The latter is shown after dE/dx cuts were applied.

Daughter kaon (pion) candidates are selected by requiring $|n\sigma_K^{dE/dx}| < 2$ ($|n\sigma_\pi^{dE/dx}| < 2$). In addition, to improve the significance of the reconstructed D^0 signal, the kaon daughter tracks were required to have a valid hit in the TOF detector and then selected with a TOF PID cut, which is denoted as the red dashed lines in Fig. 2(c). In order to have good efficiency and considering pion identification is good enough with dE/dx only, we did not require pion to match with TOF.

III. CHARMED-HADRON RECONSTRUCTION AND RAW YIELD EXTRACTION

A. D^0 Reconstruction

D^0 and $\bar{D}^0$ mesons were reconstructed via the hadronic decay $D^0(\bar{D}^0) \rightarrow K^{\mp}\pi^{\pm}$ with a branching ratio of 3.89%. The analysis technique is the same as that used for a D^0 analysis in d + Au collisions [14]. In p + p collisions, the

mixed-events technique is not suitable for describing the background due to the large contribution of correlated jets. Therefore, two different techniques were used to reproduce the background: the like-sign and track-rotation methods. Since the π^- and π^+ production is symmetric in the STAR uniform acceptance and their yield ratio is measured to be 0.988 ± 0.043 [27], the like-sign (LS) method is used and a pair combination with the same charged sign is expected to reproduce the background without the signal correlation. The opposite-sign backgrounds, which go into the residual background, are only several percent of the total background and will be discussed later. The track-rotation (Rot) technique has been used in many measurements [28]. This method is based on the assumption that by rotating the daughter kaon track by 180° in azimuth, the decay kinematics are destroyed. Thus the invariant mass distribution after rotation is able to reproduce the random combinatorial background. Figure 3 shows the invariant mass distributions of $K\pi$ candidates. Figure 3(a) shows the invariant mass distributions for $K\pi$ pairs [$0.6 < p_T(K\pi) < 2.0$ GeV/c] with unlike sign (US) before background subtraction, with like sign, and with rotated kaon momentum. The distributions from the like-sign and track-rotation techniques describe the background well. Figure 3(b) is the unlike-sign $K\pi$ invariant mass distribution after combinatorial background subtraction. A significant $K^*(892)$ peak is observed. The secondary small peak at about 1.4 GeV/c^2 is the $K_2^*(1430)$. A direct zoom-in view of the vicinity around the D^0 mass region is shown in Fig. 4 [panel (a) for subtraction of like-sign background, and panel (b) for the rotational case]. Solid symbols depict the same distributions as shown in Figs. 3 and 5 in two different D^0 p_T bins. One can see there is still some "residual" background after like-sign or rotational background subtraction. The possible sources to the residual background have been investigated using PYTHIA simulations. We performed the same reconstruction as we did on the data, for the foreground and background distributions.

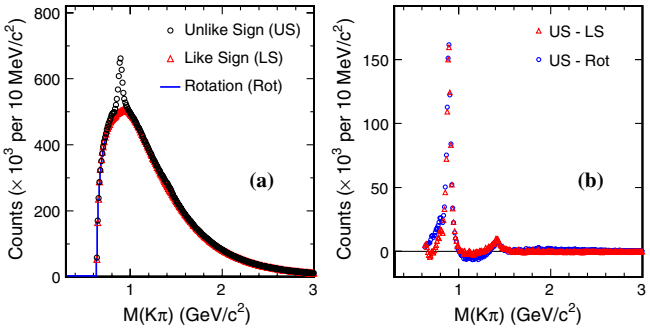

FIG. 3 (color online). (a) Invariant mass distributions of raw $K\pi$ combinations for unlike-sign pairs (circles), like-sign pairs (triangles), and kaon momentum rotated pairs (line). (b) Residual distributions after subtracting the like-sign distribution (triangles) and rotation pair distribution (dots) from the unlike-sign distribution.

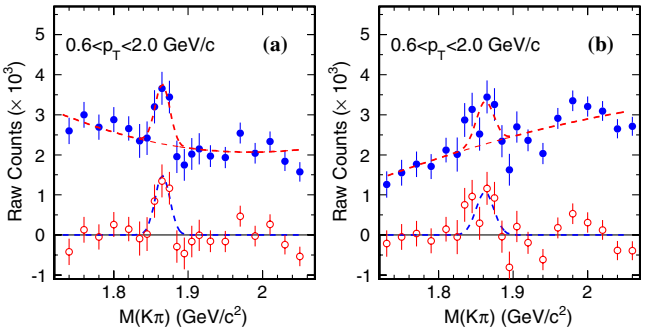

FIG. 4 (color online). Invariant $K\pi$ mass distributions in the D^0 mass region after like-sign (a) and track-rotation (b) background subtraction. Solid circles show the signal and a residual background. A Gaussian function and a second-order polynomial function were used to describe the signal and residual background, respectively. Open circles show the signal after residual background subtraction.

From these simulations, we have learned that the possible sources that can contribute to this residual correlated background include: correlated hadron pairs from decays (mostly resonances) where the real daughters were misidentified as $K\pi$ pairs; $K\pi$ pair from other decay channels of D^0 (e.g. $K^-\pi^+\pi^0$) where the other daughters are missed in the reconstruction; same-charge $K^-\pi^-$ pairs from multibody decays of $D^0 \to K^-\pi^+\pi^+\pi^-$; $K\pi$ pairs from jet fragmentations; etc. The different shape of the residual background from LS and Rot background subtraction in the data can be qualitatively reproduced by PYTHIA simulation. The magnitude of the residual background depends

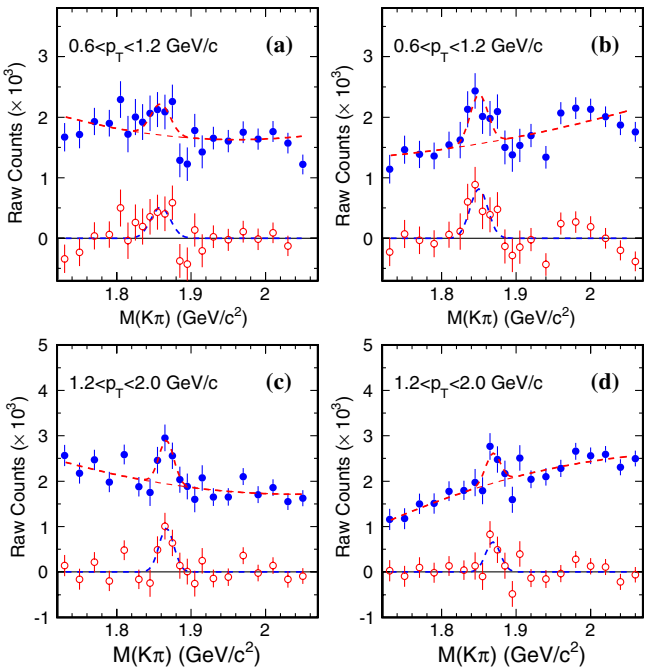

FIG. 5 (color online). Raw D^0 signals in different p_T bins after like-sign (a),(c) and track-rotation (b),(d) subtraction.

TABLE I. D^0 raw yields.

p_T range (GeV/c)	0.6–1.2	1.2–2
p_T (GeV/c)	0.908	1.57
Raw yields $\times 10^3$ (Rot)	2.45 ± 0.66	1.65 ± 0.63
Raw yields $\times 10^3$ (LS)	1.67 ± 0.74	2.40 ± 0.64

on how to choose the normalization for the like-sign or rotational background, as qualitatively understood from the PYTHIA simulations. However, the change of the residual background magnitude due to different normalizations has a very small impact on the final extracted signal counts, and it has been included in the systematic uncertainties. We used an empirical polynomial function to describe it and the choice of this empirical function was also included as one of the systematic source to the raw yields. A Gaussian function is used to fit the signal. The raw yield of the D^0 is obtained by fitting the data (blue solid circles) with a fit function representing the sum of signal and background (red dashed curve) in the mass region of $1.72 < M_{K\pi} < 2.05$ GeV/c^2. The signal after the residual background subtraction is shown as the red open circles. The Gaussian function used to describe the signal is shown as the blue dashed curve. The total D^0 signal consists of 4085 ± 938 counts.

The signals after background subtraction for two p_T bins are shown in Fig. 5. Panels (a), (c) and (b), (d) show the signals from LS and Rot background subtraction, respectively. The D^0 raw yields and statistical errors extracted from the two background methods are listed in Table I. The average values of the D^0 counts from the LS and Rot background methods are used to calculate the final D^0 raw yield in each p_T bin. The mean and width from the Gaussian fits are compared with Monte Carlo (MC) simulation in Fig. 6 (left panels). The single D^0 and D^* are embedded into the real data and simulated in the full STAR GEANT reconstruction chain, taking into account detector response and material effect. The D^0 signal mean value from an open-parameter fit shifts to lower mass due to kaon energy loss at low p_T, which is not fully accounted in the simulation due to possibly missing material budget. The systematic uncertainty in determining the D^0 raw yields as well as the potential double-counting issue due to particle misidentification will be discussed in Sec. VA.

B. D^* Reconstruction

$D^{*\pm}$ mesons were reconstructed via the decay sequence $D^{*+} \to D^0\pi^+$(BR = 67.7%), $D^0 \to K^-\pi^+$ and its charge conjugate. We followed the same analysis technique as described in Ref. [29]. The daughter particles were still identified by dE/dx in the TPC because (a) most of the D^* decay daughter particles that fall inside the STAR acceptance with higher momenta are located in the region where the TOF PID improvement is very limited and (b) the

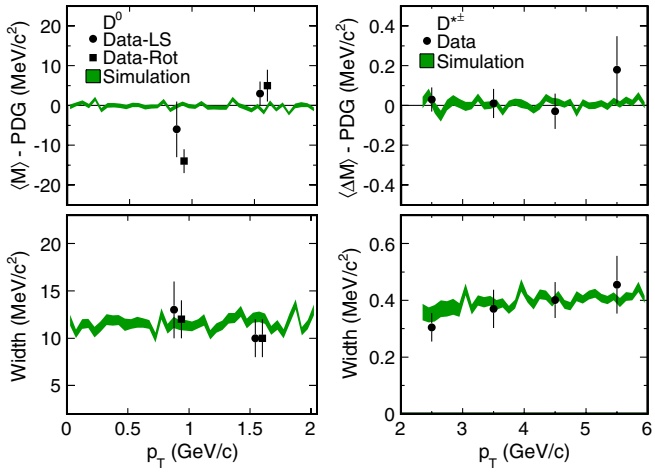

FIG. 6 (color online). The mean and width from Gaussian fit to data (symbols) compared with MC simulations (bands) for D^0 and D^* are shown in left and right panels, respectively.

signal suffers significant losses due to incomplete TOF acceptance in 2009. Compared to the cuts used in Ref. [29], the p_T threshold cut for the π^+ (from D^* decays), denoted as π_s^+, was lowered to 0.15 GeV/c. The ratio r of transverse momenta from the D^0 and π_s^+ was required to be $7 < r < 20$. These two changes were implemented to improve the statistics near the lower bound in p_T. The remainder of the analysis cuts were the same as those used in Ref. [29].

The invariant mass difference $\Delta M = M(K\pi\pi) - M(K\pi)$ was calculated in reconstructing the D^* signal to take advantage of the partial cancellation in the detector resolution in measured mass distributions. The ΔM distributions are shown in the upper panel of Fig. 7. The "right-sign" combinations $K^\mp\pi^\pm\pi_s^\pm$ were used to select the $D^{*\pm}$ candidates. Two independent methods—"wrong-sign" combinations $K^\pm\pi^\mp\pi_s^\pm$ and D^0 "sideband" combinations—were used for combinatorial background reconstruction. The plot illustrates that both methods reproduce the combinatorial background very well. The events displayed in this figure are all minimum-bias events without event-vertex selections, which demonstrates the significance of D^* signal. The lower panel in Fig. 7 shows the $K\pi$ invariant mass distribution after requiring the D^* candidate cut $(0.144 < \Delta M < 0.147$ GeV/$c^2)$. The cross-hatched area indicates D^0 candidate mass selection in the $K\pi\pi$ right-sign and wrong-sign combination reconstruction. The line-hatched area indicates the D^0 sideband region $[1.72 < M(K\pi)/(\text{GeV}/c^2) < 1.80$ or $1.92 < M(K\pi)/(\text{GeV}/c^2) < 2.00]$ used in sideband combinatorial background reconstruction for D^*. The sideband combinatorial background was used to obtain the raw D^* yields for better statistics and also because sideband distributions do not suffer from the double-counting issue due to particle misidentification. The difference between the yields obtained from the sideband method and the

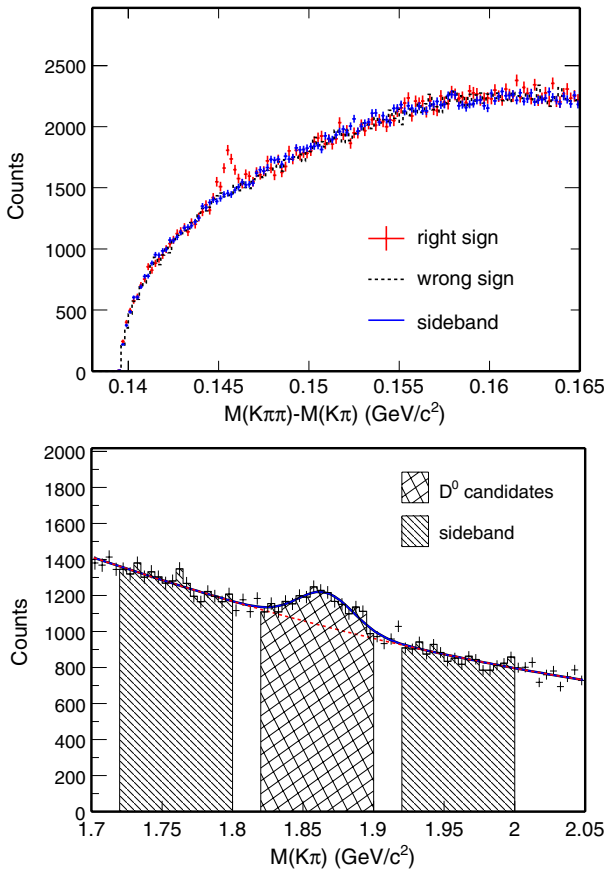

FIG. 7 (color online). Upper: Raw D^* candidate signal from the right-sign combinations in all $p+p$ minimum-bias events. Histograms are combinatorial background distributions from wrong-sign and sideband methods. Lower: Raw D^0 candidates after requiring the D^* candidate cut ($0.144 < \Delta M < 0.147$ GeV/c^2).

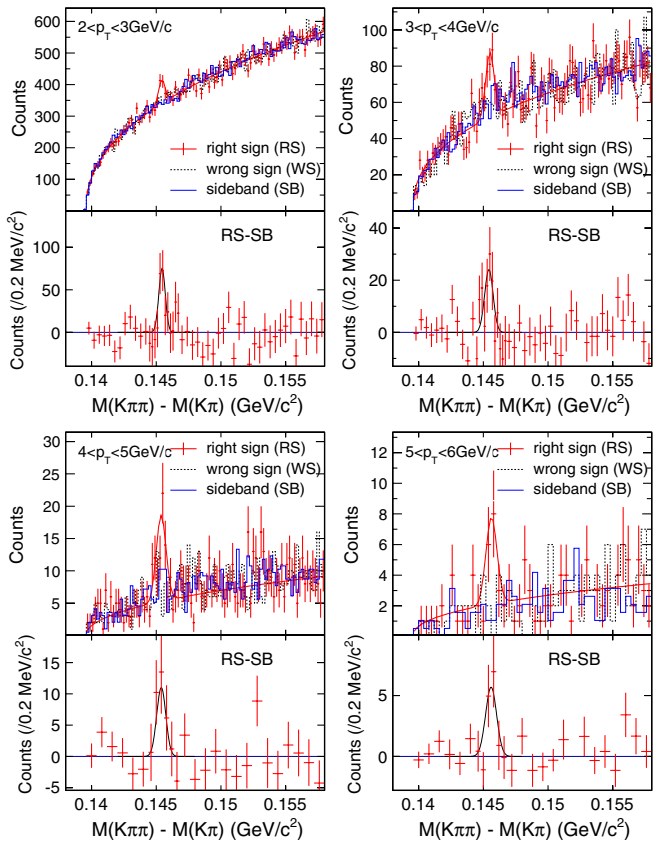

FIG. 8 (color online). Raw D^* signals in different p_T bins. In each plot, the bottom panel distribution is generated by subtracting the sideband background from the right-sign distribution. Variable binning is used in the bottom panel for better illustration.

wrong-sign method was included in the systematic uncertainties. Details in determining the uncertainties on the raw D^* yields including the double-counting effect will be discussed in Sec. VA. The D^* raw yields are summarized in Table II.

To obtain the cross section, the event-selection criteria described in the previous section were applied. The raw distributions were further divided into p_T slices to obtain the raw D^* yields in each p_T bin. Figure 8 shows the D^* candidates and background distributions in different p_T bins. The bottom panel on each plot was generated by subtracting the sideband background from the right-sign candidates. The mean and width from Gaussian fits are compared with MC simulation in the right panel of Fig. 6,

TABLE II. D^* raw yields.

p_T range (GeV/c)	2–3	3–4	4–5	5–6
p_T (GeV/c)	2.45	3.44	4.45	5.45
Raw yields	209 ± 58	98 ± 35	27 ± 11	12.3 ± 4.1

and it shows the obtained D^* peak positions and widths agree with the MC simulation well. From this analysis, the total signal consisted of 364 ± 68 counts, and the raw yield ratio of D^{*-}/D^{*+} is 0.93 ± 0.37.

IV. EFFICIENCY AND TRIGGER OR VERTEX BIAS CORRECTION

The final charmed-hadron cross section in $p+p$ collisions is calculated as follows:

$$E\frac{d^3\sigma}{dp^3} = \frac{1}{2\pi}\cdot\frac{1}{\epsilon_{\rm rec}}\cdot\frac{1}{\rm BR}\cdot\frac{\Delta N_D}{p_T\Delta p_T\Delta y}\cdot\frac{\sigma_{\rm NSD}}{N_{\rm MB}}\cdot f_{\rm trg,vtx}, \quad (3)$$

where $\sigma_{\rm NSD}$ is the total nonsingly diffractive (NSD) cross section, which is measured at STAR to be 30.0 ± 2.4 mb [30]. $N_{\rm MB}$ is the total number of minimum-bias events used for the analysis. ΔN_D is the raw charmed-hadron signal in each p_T bin within a rapidity window Δy. BR is the hadronic decay branching ratio for the channel of interest. There are two correction factors: $\epsilon_{\rm rec}$, which is the reconstruction efficiency including geometric acceptance, track selection efficiency, PID efficiency, and analysis cut efficiency; and $f_{\rm trg,vtx}(p_T)$, which is the correction factor to

account for the bias between the minimum-bias sample used in this analysis and the total NSD sample. This bias is mainly caused by the VPD trigger and event-vertex reconstruction, and it may have a dependence on the charmed-hadron p_T. In the following sections of the paper, the condition that requires the event to fire the VPD trigger and to have a good vertex will be referred to as the "analysis condition."

A. Reconstruction efficiency

The reconstruction efficiency for charmed hadrons was obtained by embedding MC simulated charmed-hadron tracks into the real minimum-bias events. The MC charmed-hadron tracks were processed through a full GEANT detector simulation [31] with a representation of the 2009 STAR geometry. The raw detector-response signals were mixed together with those from the real data and processed through the full STAR offline reconstruction chain to obtain the detector-response efficiency in a realistic environment. The input MC track multiplicity was constrained to have negligible effect on the final tracking efficiency due to increased occupancy in the TPC.

Figures 9 and 10 show the D^0 and D^* reconstruction efficiency versus p_T within $|y| < 1$. In Fig. 9, the solid squares denote the reconstruction efficiency for both daughters selected and identified by the TPC, while the solid circles denote the reconstruction efficiency with additional PID selection from the TOF detector for the kaon daughter. The combined TOF efficiency, including the acceptance, matching between TPC tracks and TOF hits, and PID selection efficiency, is around 45% studied from the data in 2009.

B. Trigger and vertex bias corrections

The trigger and vertex bias corrections were studied by simulating PYTHIA events [19] processed through the full GEANT detector-response and offline reconstruction. The PYTHIA generator versions 6.205 and 6.416 were both used

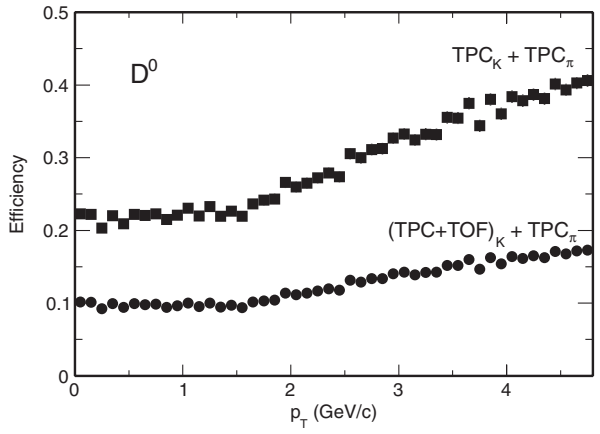

FIG. 9. Total D^0 reconstruction efficiency versus $D^0 p_T$.

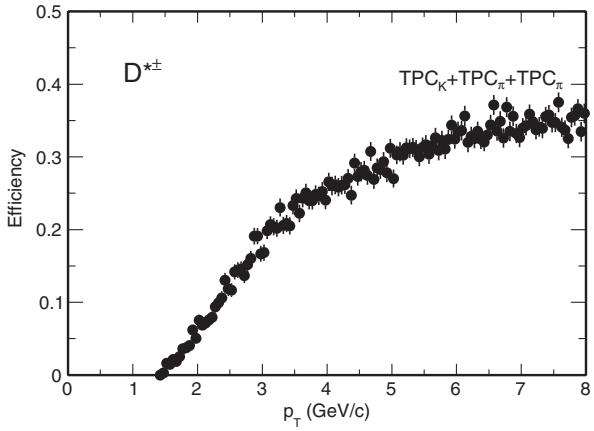

FIG. 10. Total D^* reconstruction efficiency versus $D^* p_T$.

in this study. We chose the PYTHIA version 6.205 with minimum-bias processes selected and with the CDF TUNEA settings [32] to give the centroid value of the correction factor because it gives better description for the particle production in the forward rapidities than the 6.416 version [33]. The differences between the two versions as well as different parameter settings have been included to estimate the systematic uncertainty of the trigger and vertex bias correction factor.

To validate the PYTHIA generator in simulating particle production in the forward region for the VPD trigger study, we first compared the VPD trigger efficiencies (from the BBC triggered minimum-bias sample) from MC simulation and real data. The BBC trigger has been well studied and was used to calculate the $p + p$ NSD cross section [16]. Figure 11 shows the comparison of the VPD trigger efficiency, with the requirement that there is a BBC trigger and a good vertex. The efficiency is studied as a function of the charged hadron p_T. The real data used are BBC triggered minimum-bias events taken in 2009 during a very low luminosity run, which minimizes TPC pileup tracks.

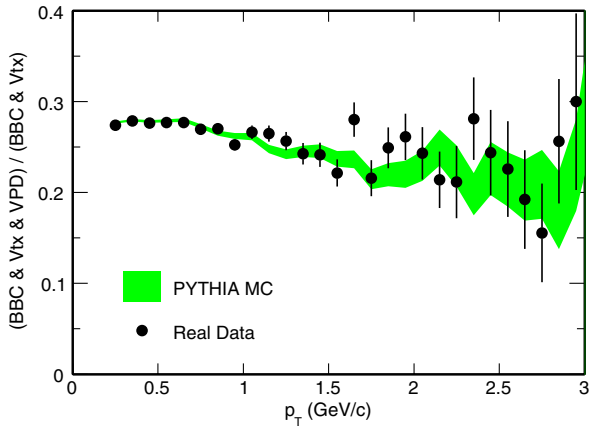

FIG. 11 (color online). VPD trigger efficiency comparison between data and Monte Carlo versus charged-particle p_T in BBC minimum-bias conditions.

Figure 11 shows that the efficiency goes down with increasing p_T of midrapidity particles indicating an anticorrelation between midrapidity particle production and forward VPD triggering. Most importantly, within the momentum range under study, the PYTHIA MC simulation agrees well with the data. This agreement provides confidence in using PYTHIA simulations to evaluate this correction.

The correction factor $f_{\mathrm{trg,vtx}}$ can be related to the ratio (N_D/N_{mb}) for the pure minimum-bias condition and the analysis condition, i.e.

$$f_{\mathrm{trg,vtx}}(p_T) \equiv \frac{N_D(p_T)/N_{\mathrm{mb}}}{N_D^{\mathrm{trg,vtx}}(p_T)/N_{\mathrm{mb}}^{\mathrm{trg,vtx}}}. \tag{4}$$

Two simulation samples were generated to obtain the correction factor. One sample consisted of PYTHIA-simulated $p + p$ events and was used to obtain the fraction of minimum-bias events that satisfy the analysis condition $N_{\mathrm{mb}}^{\mathrm{trg,vtx}}/N_{\mathrm{mb}}$. This fraction was found to be 12.7% from this PYTHIA simulation. The other simulation sample was generated using the same PYTHIA settings, but only events with at least one charmed hadron were saved to enhance the statistics. This sample was used to obtain the fraction of charmed-hadron signals that satisfy the analysis condition $N_D^{\mathrm{trg,vtx}}/N_D$. We also studied this fraction as a function of charmed-hadron p_T. Figure 12 shows the calculated efficiencies for D^* from different event-selection criteria. The BBC coincidence study provides a baseline for this simulation, which demonstrates consistency with previous STAR results [30]. As expected, the vertex finding efficiency increases with increasing p_T. The VPD trigger efficiency shows an anticorrelation with increasing $D^* p_T$, similar to that observed with increasing charged-hadron p_T. The final efficiency (with requirements for both vertexing and VPD triggering) is almost flat versus p_T, leveling off at ~19%. The simulation for D^0 hadrons shows very

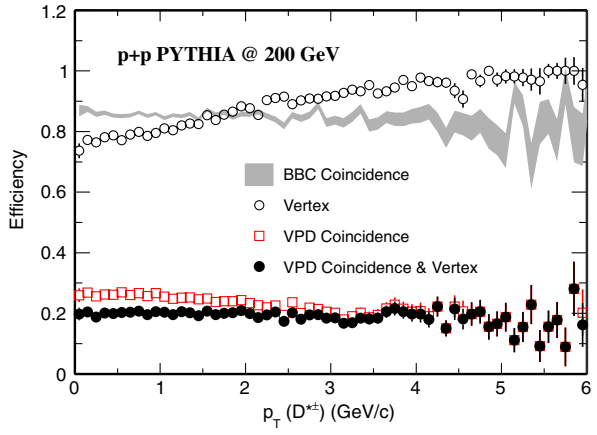

FIG. 12 (color online). D^* efficiency versus D^* p_T with different event-selection criteria.

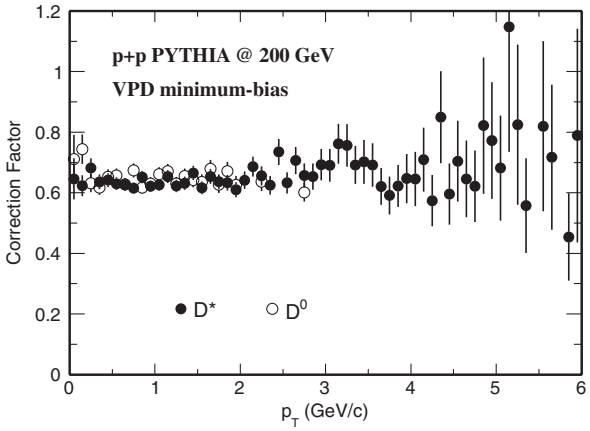

FIG. 13. The correction factor $f_{\mathrm{trg,vtx}}$ versus charmed-hadron p_T for cross section calculations for D^0 and D^*.

similar results. Figure 13 shows the correction factor $f_{\mathrm{trg,vtx}}$ for cross section calculations for D^0 and D^*.

V. SYSTEMATIC UNCERTAINTIES

Sources that contribute to the systematic uncertainties in the final D-meson cross sections include: (a) uncertainty in determining the raw D-meson yields; (b) uncertainty in determining the reconstruction efficiency; (c) uncertainty of the total NSD cross section; and (d) uncertainty in determining the trigger or vertex correction factor. Uncertainties due to particle identifications will enter in both (a) and (b) which will be discussed in the following subsections. We consider (a) as point-by-point uncorrelated systematic uncertainties. Although (b) is correlated in p_T, it is not simply a normalization uncertainty, and the exact correlation in p_T is not known. Therefore we include (b) in the point-by-point uncorrelated systematic uncertainties. Finally, (c) and (d) are overall normalization uncertainties.

A. Uncertainty in raw yields

Different choices on background reconstruction methods, function fits and mass binning were used to evaluate the systematic uncertainty in the raw D-meson yields. In the D^0 analysis, the difference between the yields extracted from Rot and LS methods is 15.6%–18.9%. Fitting the D^0 peak with fixed parameters from simulation estimates lower yields of 28.2% and 6.1% for the two D^0 p_T bins. The systematic uncertainties from different mass binning and different fit regions are estimated to be ~5%–7%. The systematic uncertainties in determining the raw D^* yields include contributions from the difference obtained between the sideband and the wrong-sign methods, and the difference between bin counting and Gaussian fitting methods, varying ~6%–11% in the p_T range 2–6 GeV/c. The choice of mass binning and fitting range had a negligible effect on the extracted yields.

In D^0 meson reconstruction, if the kaon (pion) daughter is misidentified as a pion (kaon), then two daughters from a real D^0 decay will show up as additional $\bar{D}^0$ combinations with a wider mass distribution due to wrong mass assignments. Thus one D^0 signal will be counted twice, once as a D^0 and again as a $\bar{D}^0$. A Monte Carlo simulation was used to evaluate the fraction of such double-counting occurrences in the D^0 reconstruction. Based on realistic dE/dx and TOF PID resolutions extracted from real data, the probability that kaons (pions) can be misidentified as pions (kaons) at a given p_T, using these PID selections, was obtained. Assuming a D^0 candidate, this procedure provides an estimate of the probability that both daughters are misidentified and then reconstructed as a $\bar{D}^0$. In Fig. 14, the open and closed circles show the double-counting fraction, relative to the total real signal, for two different PID selections: (a) both daughters are identified by TPC dE/dx; (b) the kaon daughters are identified by the TOF, while pions are identified by the TPC. The sharp increase at very low p_T (identifying both daughters using dE/dx) is due to the case where a D^0 decays almost at rest ($p_T \sim 0$), and the two daughters are produced in the momentum region where the kaon and pion dE/dx bands cross, therefore maximizing the misidentification probability. The plot shows that when the kaon daughter is identified by the TOF, the double-counting fraction is negligible in our D^0 p_T coverage region (0.6–2.0 GeV/c).

Double counting the D^0 may also impact reconstruction of D^*. However, the impact is different because of a charge sign requirement on the soft pions. If both daughters from a D^0 are misidentified (D^0 is reconstructed as $\bar{D}^0$), then the combination from the same signal will become $K^+\pi^-\pi^+$. It will not contribute to the right-sign distributions but, instead, will enter into the wrong-sign (background) distributions if the mass also falls into the D^0 ($\bar{D}^0$) mass selection window. Thus the double counting in wrong-sign background will contribute to an undercounting in the total signal if the wrong-sign background is subtracted from the right-sign distribution. Since the right-sign combination was also required, the misidentification does not affect the sideband background distributions. In the real analysis, the sideband background subtraction was used to extract the raw signal, but also the difference between sideband and wrong-sign methods was used for systematic uncertainty estimation. Since the wrong-sign distribution can be overestimated due to particle misidentification, the systematic error from the difference between the two methods would be overestimated. This was avoided with better understanding of the wrong-sign overcounting. The red triangles in Fig. 14 denote the overcounting fraction in the D^* wrong-sign background to real signals. It is very close to the D^0 double-counting fraction, since they are from the same source. The slight difference comes from the additional D^0 candidate selection cuts used in the D^* reconstruction. This fraction was used to compensate for the difference between the two background methods and as a way to improve the assessment of the systematic uncertainties in the extraction of the raw D^* yields.

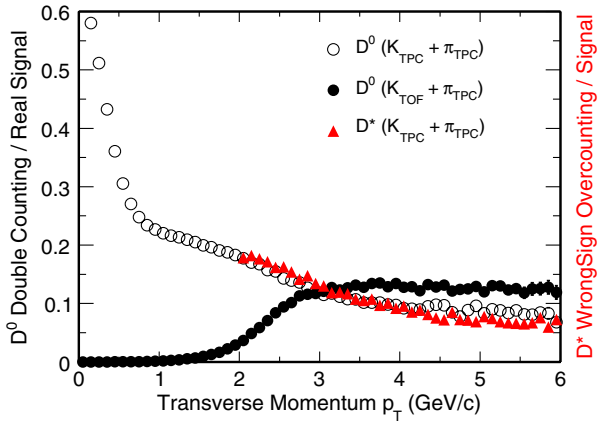

FIG. 14 (color online). D^0 double-counting fraction due to particle misidentification in two PID selections and D^* wrong-sign over counting fraction versus D-meson p_T.

B. Uncertainty in reconstruction efficiency

The systematic uncertainties of the reconstruction efficiencies were obtained following similar methods used in other particle cross section measurements by changing the daughter track selection criteria and comparing the difference between the data and the MC. In this analysis, it was studied by changing the minimum number of fit points (nFitPts) in the TPC from 15 to 25 and the DCA to the collision vertex from 2 to 1 cm. The uncertainty was then quantified by the difference in the remaining fractions after cut changes between the data and the MC. For each cut change, the uncertainties were calculated for each decay daughter and added together linearly to obtain the total for D^0 and D^*. The systematic uncertainties on the PID cut efficiencies (from both dE/dx and TOF) were estimated to be $<1\%$ and neglected in the total uncertainty. Then the uncertainties from the cut changes on nFitPts and DCA were added in quadrature to obtain the total systematic uncertainty on the reconstruction efficiency.

The point-by-point systematic errors including uncertainties in raw yields and reconstruction efficiency for the D^0 and D^* cross sections in each p_T bin are summarized in Table III.

TABLE III. D^0 (0.6–2 GeV/c) and D^* (2–6 GeV/c) point-by-point systematic errors (%).

p_T (GeV/c)	0.6–1.2	1.2–2	2–3	3–4	4–5	5–6
Raw yields	$^{+18.9}_{-33.9}$	$^{+15.6}_{-16.8}$	9.4	6.5	11.0	6.6
nFitPts 15 → 25	3.8	3.2	7.2	4.7	5.9	4.7
DCA 2 → 1 (cm)	6.6	7.1	13.6	12.7	11.6	10.7
Quadratic sum	$^{+20.8}_{-34.8}$	$^{+17.8}_{-18.5}$	18.1	15.1	17.1	13.5

C. Overall normalization uncertainty

The overall normalization uncertainty for the total NSD cross section has been studied before and reported in a previous STAR publication [30]. It was estimated to be 8.1%, including the uncertainty from measuring the absolute BBC cross section and that of BBC triggering efficiency. The uncertainty from the trigger or vertex bias correction factor amounts to 5.2% by varying different PYTHIA versions (6.205 vs 6.416) and different parameter settings in the simulation. We also considered the impact from pileup TPC tracks as an additional systematic source on the correction factor, and the uncertainty was estimated to be 4.0% by comparing the result with a conservative luminosity level for this data set to that from pure PYTHIA simulation without pileup.

These uncertainties were added in quadrature, which gives 10.4% overall normalization uncertainty for the D-meson cross sections.

VI. RESULT AND DISCUSSION

After the reconstruction efficiency and trigger or vertex bias correction factor were applied, the differential production cross sections for D^0 and D^* in $p + p$ collisions at $\sqrt{s} = 200$ GeV were extracted, as shown in Fig. 15. The vertical bars on the data points indicate the statistical uncertainties, while the brackets indicate the bin-to-bin systematic uncertainties described in the previous section. The D^0 and D^* cross sections were divided by the charm quark fragmentation ratios 0.565 ± 0.032 ($c \to D^0$) and 0.224 ± 0.028 ($c \to D^{*+}$), respectively, to convert to the $c\bar{c}$ production cross section. The charm quark fragmentation ratios are measured from CLEO and BELLE experiments near the Υ resonance [34]. The uncertainties of the fragmentation ratios are taken into account as systematic errors in calculating the $c\bar{c}$ production cross section. A power-law fit to the data points was performed with the following function [14]:

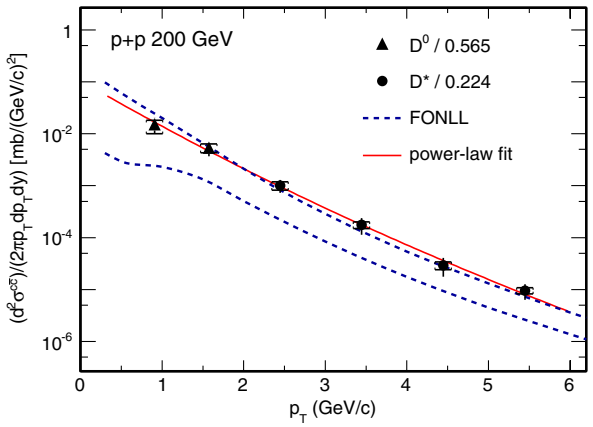

FIG. 15 (color online). $c\bar{c}$ production cross section as inferred from D^0 and D^* production in $p + p$ collisions at $\sqrt{s} = 200$ GeV compared with FONLL calculations. The D^0 and D^* data points were divided by the charm quark fragmentation ratios 0.565 ($c \to D^0$) and 0.224 ($c \to D^{*+}$) [34], respectively, to convert to the $c\bar{c}$ production cross section.

$$E\frac{d^3\sigma}{dp^3} = \frac{d\sigma}{dy}\frac{2(n-1)(n-2)}{\pi(n-3)^2\langle p_T\rangle^2}\left(1 + \frac{p_T}{\langle p_T\rangle(n-3)/2}\right)^{-n} \tag{5}$$

and shown as the solid red line in the figure. The fit quality with the power-law function, measured as χ^2/ndf, is $0.9/3$ with statistical errors and $3.7/3$ with point-by-point systematic errors, respectively. The latter was used to extract the systematic uncertainty on the p_T integrated cross section from point-by-point systematic sources. The obtained $c\bar{c}$ production cross section at midrapidity is

$$\left.\frac{d\sigma}{dy}\right|_{y=0}^{c\bar{c}} = 170 \pm 45(\mathrm{stat})^{+38}_{-59}(\mathrm{sys})\ \mu\mathrm{b}. \tag{6}$$

The term with sys includes the uncertainty arising from the bin-to-bin systematic uncertainties and from the extrapolation to the low-p_T region, which is not measured. The FONLL upper limit and PYTHIA + tune fits are used for the low-p_T extrapolation, which gives $+6.2\%$ and -16.4% uncertainties, respectively. At midrapidity, about 67% of the D meson yield falls in the measured p_T region. The mean transverse momentum of charmed mesons is found to be $1.06 \pm 0.14(\mathrm{stat}) \pm 0.09(\mathrm{sys})$ GeV/c. The charm-pair cross section at midrapidity from this measurement is consistent with STAR's previous measurement in d + Au collisions [14] at 1.7σ (σ is the averaged total uncertainty between two results), providing negligible nuclear effects in d + Au collisions.

Also shown in Fig. 15 are the upper and lower edges (blue dashed lines) of a FONLL pQCD calculation taken from Ref. [9]. Our results are consistent with the upper limit of the FONLL pQCD calculation in a wide p_T region. It is observed that the charmed-hadron cross sections measured by CDF [13] and ALICE [35] at energies up to 7 TeV are also close to the upper limits of FONLL pQCD calculations. This may help set constraints on the parameters used in the FONLL calculations, e.g. on the choice of renormalization or factorization scales, which are the main parameters varied to obtain the upper and lower limits on these calculations. However one should note the valid p_T region of FONLL calculations when applying such an analysis since FONLL calculations are supposed to work when $p_T \gg m_c$.

The charm cross section at midrapidity was extrapolated to full phase space using the same extrapolation factor, 4.7 ± 0.7, as in a previous publication [14], and the extracted charm total cross section at $\sqrt{s} = 200$ GeV is

$$\sigma_{c\bar{c}} = 797 \pm 210(\mathrm{stat})^{+208}_{-295}(\mathrm{sys})\ \mu\mathrm{b}. \tag{7}$$

Shown in Fig. 16, the data were also compared with PYTHIA calculations. PYTHIA version 6.416 was used as it has been tuned to describe the midrapidity Tevatron data.

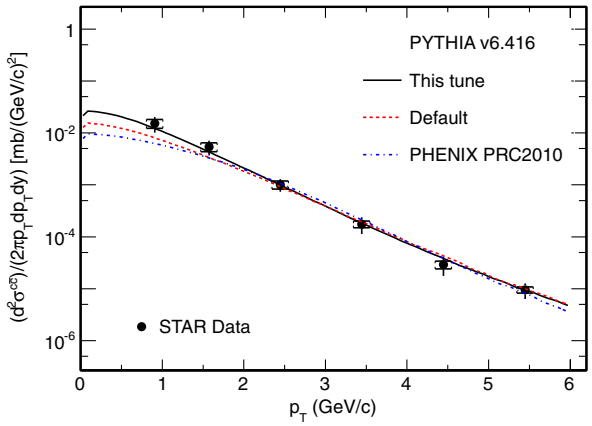

FIG. 16 (color online). $c\bar{c}$ production cross section as inferred from D^0 and D^* production in $p+p$ collisions at $\sqrt{s} =$ 200 GeV compared with PYTHIA calculations. Data are fitted with PYTHIA spectra with an overall scale parameter for the purpose of shape comparison only.

We tried PYTHIA calculations with the following sets of parameters to compare with our measurements:

(a) Default MSEL = 1.

(b) PHENIX tune: MSEL = 0 with MSUB(11, 12, 13, 28, 53, 68) on, PARP(91) ($\langle k_\perp \rangle$) = 1.5 GeV/c, MSTP(32) (Q^2 scale) = 4, CKIN(3) (min. parton $\hat{p}_\perp$) = 2 GeV.

(c) This tune: MSEL = 1, PARP(91) ($\langle k_\perp \rangle$) = 1.0 GeV/c, PARP(67) (parton shower level) = 1.0.

The choice of modifying the primordial $\langle k_\perp \rangle$ (the Gaussian width of primordial k_T in hadrons) and the parton shower level parameters from default values (2 GeV/c and 4, respectively) in this tune was suggested by the matching of scales in heavy-flavor production at lower energies [36], which has been noted in PYTHIA [19]. The CDF TUNEA parameters [32], which were tuned to reproduce midrapidity jet and "underlying event" results at Tevatron energies, are included as defaults in PYTHIA v6.416. "PHENIX tune" parameters are those used in the PHENIX charm continuum contribution estimation from dielectron measurements [37]. The default parton distribution function (CTEQ5L) was used in all three cases.

All ground-state charmed hadrons (D^0, D^+, D_s^+, and Λ_c^+) were added together in the rapidity window $|y| < 1$ to obtain charm cross sections. The data were then fitted with the PYTHIA calculations with an overall scale factor as the unique free parameter. The charm production p_T spectrum with this tune gives best χ^2: 1.41 (this tune), 4.97 (default), 5.96 (PHENIX tune). This is the first direct D-meson measurement that goes down to such a low p_T, which constrains the model parameters better.

VII. SUMMARY

In summary, measurement on the charmed meson (D^0 and D^*) production cross sections via their hadronic decays in $p+p$ collisions at $\sqrt{s} = 200$ GeV has been reported. The charm-pair production cross section at midrapidity extracted from this analysis is $d\sigma/dy|_{y=0}^{c\bar{c}} = 170 \pm 45(\text{stat})^{+38}_{-59}(\text{sys})$ μb. The charm total cross section at $\sqrt{s} =$ 200 GeV is estimated as $797 \pm 210(\text{stat})^{+208}_{-295}(\text{sys})$ μb. The reconstructed charmed mesons cover the p_T range 0.6–6 GeV/c. The charm-pair transverse momentum differential cross sections from this analysis are consistent with the upper bound of a fixed-order next-to-leading logarithm perturbative QCD calculation. When comparing to PYTHIA model calculations, we found that a calculation with smaller primordial $\langle k_\perp \rangle$ and parton shower level compared to CDF TUNEA settings describes the shape of the p_T distribution of data.

ACKNOWLEDGMENTS

We thank the RHIC Operations Group and RCF at BNL, the NERSC Center at LBNL and the Open Science Grid consortium for providing resources and support. This work was supported in part by the Offices of NP and HEP within the U.S. DOE Office of Science, the U.S. NSF, the Sloan Foundation, the DFG cluster of excellence "Origin and Structure of the Universe" of Germany, CNRS/IN2P3, FAPESP CNPq of Brazil, Ministry of Education and Science of the Russian Federation, NNSFC, CAS, MoST, and MoE of China, GA and MSMT of the Czech Republic, FOM and NWO of the Netherlands, DAE, DST, and CSIR of India, Polish Ministry of Science and Higher Education, Korea Research Foundation, Ministry of Science, Education and Sports of the Republic of Croatia, and RosAtom of Russia.

[1] J. Adams *et al.* (STAR Collaboration), Nucl. Phys. **A757**, 102 (2005).

[2] Z. Lin and M. Gyulassy, Phys. Rev. C **51**, 2177 (1995); **52**, 440(E) (1995).

[3] B. Mueller, Nucl. Phys. **A750**, 84 (2005).

[4] G. D. Moore and D. Teaney, Phys. Rev. C **71**, 064904 (2005).

[5] H. van Hees and R. Rapp, Phys. Rev. C **71**, 034907 (2005); R. Rapp and H. van Hees, arXiv:0803.0901.

[6] J. Uphoff, O. Fochler, Z. Xu, and C. Greiner, Phys. Rev. C **82**, 044906 (2010).

[7] R. L. Thews, M. Schroedter, and J. Rafelski, Phys. Rev. C **63**, 054905 (2001).

[8] A. Andronic, P. Braun-Munzinger, K. Redlich, and J. Stachel, Phys. Lett. B **571**, 36 (2003).

[9] M. Cacciari, P. Nason, and R. Vogt, Phys. Rev. Lett. **95**, 122001 (2005).

[10] R. Vogt, Eur. Phys. J. Special Topics **155**, 213 (2008).

[11] S. P. K. Tavernier, Rep. Prog. Phys. **50**, 1439 (1987).

[12] X. Dong, Ph.D. thesis, University of Science and Technology of China, 2005, arXiv:nucl-ex/0509011, Appendix C and references therein.

[13] D. Acosta *et al.* (CDF Collaboration), Phys. Rev. Lett. **91**, 241804 (2003).

[14] J. Adams *et al.* (STAR Collaboration), Phys. Rev. Lett. **94**, 062301 (2005).

[15] B. I. Abelev *et al.* (STAR Collaboration), Phys. Rev. Lett. **106**, 159902(E) (2011).

[16] H. Agakishiev *et al.* (STAR Collaboration), Phys. Rev. D **83**, 052006 (2011).

[17] A. Adare *et al.* (PHENIX Collaboration), Phys. Rev. Lett. **97**, 252002 (2006).

[18] S. S. Adler *et al.* (PHENIX Collaboration), Phys. Rev. Lett. **96**, 032301 (2006); A. Adare *et al.* (PHENIX Collaboration), Phys. Rev. Lett. **98**, 172301 (2007).

[19] T. Sjöstrand, S. Mrenna, and P. Skands, J. High Energy Phys. 05 (2006) 026.

[20] Special Issue on RHIC and Its Detectors, edited by M. Harrison, T. Ludlam, and S. Ozaki [Nucl. Instrum. Methods Phys. Res., Sect. A **499**, No. 2–3 (2003)].

[21] M. Anderson *et al.*, Nucl. Instrum. Methods Phys. Res., Sect. A **499**, 659 (2003).

[22] STAR TOF proposal, http://drupal.star.bnl.gov/STAR/files/future/proposals/tof-5-24-2004.pdf.

[23] M. Beddo *et al.*, Nucl. Instrum. Methods Phys. Res., Sect. A **499**, 725 (2003).

[24] C. E. Allgower *et al.*, Nucl. Instrum. Methods Phys. Res., Sect. A **499**, 740 (2003).

[25] W. J. Llope, in *Proceedings of 24th Winter Workshop on Nuclear Dynamics, 2008* (unpublished).

[26] J. Kiryluk, AIP Conf. Proc. **675**, 424 (2003).

[27] B. I. Abelev *et al.* (STAR Collaboration), Phys. Rev. C **79**, 034909 (2009).

[28] C. Adler *et al.* (STAR Collaboration), Phys. Rev. Lett. **89**, 132301 (2002); J. Adams *et al.* (STAR Collaboration), Phys. Rev. Lett. **95**, 122301 (2005); Phys. Rev. C **70**, 44902 (2004); B. I. Abelev *et al.* (STAR Collaboration), Science **328**, 58 (2010); K. Aamodt *et al.* (ALICE Collaboration), Phys. Lett. B **704**, 442 (2011).

[29] B. I. Abelev *et al.* (STAR Collaboration), Phys. Rev. D **79**, 112006 (2009).

[30] J. Adams *et al.* (STAR Collaboration), Phys. Rev. Lett. **91**, 172302 (2003).

[31] GEANT 3.21, CERN program library. http://wwwasdoc.web.cern.ch/wwwasdoc/22geanthtml3/geantall.html.

[32] R. D. Field *et al.*, arXiv:hep-ph/0510198.

[33] N. Poljak (for the STAR Collaboration), Nuovo Cimento Soc. Ital. Fis. C **035N2**, 193 (2012).

[34] C. Amsler *et al.*, Phys. Lett. B **667**, 1 (2008).

[35] A. Dainese *et al.* (ALICE Collaboration), J. Phys. G **38**, 124032 (2011).

[36] E. Norrbin and T. Sjöstrand, Phys. Lett. B **442**, 407 (1998); Eur. Phys. J. C **17**, 137 (2000).

[37] A. Adare *et al.* (PHENIX Collaboration), Phys. Rev. C **81**, 034911 (2010), footnote in reference [51].